Chapter VII

Processing of $CuIn(S,Se)_2$ Absorber Layer for PVs Application

VII.1 Introduction

Among the 2nd generation thin film solar cells (TFSC), chalcopyrite CIGS based solar cell is one of the most promising alternatives to conventional silicon solar cells. The highest reported efficiency of thin-film CIGS solar cell is 23.35% [20], which compares well with the highest achieved efficiency of silicon solar cell (26.7%) [14]. Because of the indirect bandgap and weaker absorption, a much thicker layer (250-300μm) of silicon is required which makes silicon solar cells bulky and rigid. CIGS on the other hand, is an efficient absorber because of its direct bandgap, making it a leading candidate for flexible devices. The CIGS solar cell with efficiencies exceeding 20% has been reported by several research groups [30, 123, 280, 281]; however, these high-efficiency devices have been processed through cost intensive vapour-based co-evaporation and sputtering techniques. In addition, implementing these vacuum-based deposition technologies for large-scale, high-throughput production is challenging. Therefore, developing low-cost scalable solution-based processing technologies has been an active area of research for last two decades [137]; The performance of solution-processed CIGS absorber-based devices are still much lower (record PCE around 18.7% [35]) when compared to the vacuum processed ones. There are several challenges that is needed to be addressed to improve the device performance. During solution-processing, solvents

and metal precursors leave elemental impurities such as C, O, N, and Cl, which hampers the absorber performance by generating a porous layers or small grains which results in lower shunt and high series resistance. These residual impurities can be reduced by utilizing hydrazine as solvent [33, 137]; however, it cannot be applied for large scale production due to their hepatotoxic, explosive, carcinogenic nature. In addition, the presence of voids and surface roughness in the solution processed absorber layers increase surface recombination and reduce carrier collection efficiency. Generally, solution processed films have a fine-grained layer with high boundary density, which deteriorates the cell performance due to recombination at grain boundaries and/or decrease carrier mobility [39, 42, 269]. Therefore, the major challenge in high-throughput processing (spray deposition/inkjet printing/screen printing) is to obtain a high quality, uniform and integrated films with minimum crack and void. It is reported that a dense and uniform film can be deposited by carrying out the deposition in several passes depositing thinner layers at each deposition pass which minimizes the volume contraction and the formation of cracks [282].

In this chapter, we have tried to mitigate some of the stated issues and demonstrated processing of solar cell grade high density, large grained absorber layer through spray deposition. We have discussed the ink formulation and spray deposition conditions to produce homogeneous, smooth, and crack-free film from NPs based inks. Further, films were selenized to convert wz-CIS NPs films into large-grained ch-CISSe, and demonstrated a working device. The films microstructure, phase transformation, composition and chemical state due to selenization were investigated by SEM, XRD and Raman, and XPS respectively.

VII.2 A Review of Relevant Literature

CIS absorber layers have been processed using several solution based techniques including inkjet printing, chemical bath deposition (CBD), spin coating, doctor blade, spray coating and spray pyrolysis. Out of all, spray pyrolysis/coating is probably the most versatile technique that has the advantage of large area coverage, which is amenable to roll to roll processing. Dense absorber layer can be produced by depositing in multiple passes with each pass depositing a thinner layer [28]. The quality and properties of thin films processed by spray deposition depend on several parameters including substrate temperature, spray rate, nozzle distance from the substrates and ink concentration. Substrate temperature should be high enough to evaporate the solvent immediately on deposition [252]; at the same time, it shouldn't be too high to allow unwanted reaction such as formation of molybdenum oxide [60] and segregation of phases. Suhail *et al.* [283] prepared the copper-rich CIS layer, observed the formation of Cu_2S phase, which was attributed to higher substrate temperature [284]. Good uniformity, growth rate and adhesion of the deposited films were reported for the substrate temperature between 200 to 300 ^oC [60, 285, 286]. The spray rate has been reported to affect the properties such as crystallinity, surface morphology, resistivity and thickness. In general, slower spray rate around 5ml/min is preferred for the formation of crystalline films [256, 286–288]. Higher spray rates are known to produce rough surface [289] and notably, the residual oxygen and carbon impurities were relatively high in the fast-sprayed films [290]. The height of spray head influences film quality and determines the area coated per pass and deposition rate [153, 291]. High substrate to nozzle distance increases the residence time and spread of the spray resulting in premature

precipitation in flight resulting in porous films, while too low a distance, literally deposits droplets which lumps NPs precipitate forming agglomerates [256, 285, 291]. Therefore, a careful adjustment of the distance between the nozzle and the substrate is needed. Another crucial parameter is ink concentration [252]. The ink concentration decides the duration and number of pass of spraying needed to obtain the required thickness and coverage [252]. Higher ink concentration requires comparatively lesser spray time, while larger grain sizes were reported for high concentration ink [292]. Roughness of the film has been reported to increase with high concentration precursor inks [252].

Several reports have been published on the synthesis mechanism of wz-CIGS NPs describing the morphology, shape and their electrical and optical properties [175, 195, 199, 224, 239]; however, only few have studied its application as absorber layer [233, 293, 294]. Highest reported efficiency of 6.77% has been reported for a wz-CIS based solar cell (FTO/TiO2/CdS/CIS/Au) deposited by the electrophoretic technique [294]. Lower performance of the wz-CIS based solar cells is attributed to the wider bandgap, small grain size and defect concentration. Therefore, to obtained the large grained chalcopyrite phase, selenization is performed after the spray deposition [60, 260]. Selenization of wz-CIS would ensure large grained chalcopyrite phase, minimizing the defect, and thereby improving the carrier transport [15, 60] (already explained in chapter I and VI).

VII.3 Experimental Procedure

VII.3.1 Wurtzite-CIS Nanoparticle Ink Preparation

Wurtzite CIS ink preparation was carried out in two different ways:

I. 260 mg of the synthesized wz-CIS (details in chapter III) nanoparticles were dispersed in a mixture of 20 ml toluene and 1-dodecanthiol (1-DDT), where 1-DDT was varied from 2 to 8 ml.

II. Dispersing varying amount (56 and 68 mg) of wz-CIS nanoparticles in a mixture of 20 ml toluene and 2 ml 1-DDT.

VII.3.2 Processing of Absorber Layer

Spray deposition of wz-CIS Films

The prepared wz-CIS ink was stirred overnight and probe sonicated at 200 W power for 30 seconds, before deposition. The deposition of wz-CIS ink was performed using the spray pyrolysis equipment; schematic is shown in **Figure VI.1(a)**. Except substrate temperature (200-300 ^{o}C) and ink concentration, other deposition parameters such as the carrier gas pressure (1bar), nozzle-to-substrate distance (~12 cm), solution flow rate (2 ml/min), and nozzle speed (300x6) were kept constant as mentioned in chapter III and VI . In the present case, toluene and 1-DDT solvent are used as dispersant for NPs ink. Both toluene and 1-DDT is easily evaporated during the deposition of NPs on a heated surface (250°C). To further ensure the removal of organic molecules, the deposited films were heated to 400°C in inert atmosphere. Therefore, there is very less probability of the presence of any residue.

Selenization of Absorber Layer

Spray deposited wz-CIS films were selenized in a tubular furnace at temperatures 550 ℃ for 15 min. Detail of the selenization process for the formation of chalcopyrite CISSe absorber film is discussed in chapter VI.

VII.4 Fabrication of wz-CIS and ch-CISSe Device

The ink was spray-deposited on Mo-coated glass substrates with nitrogen as the carrier gas. The spraying was tuned according to the substrate temperature for required film thickness (1.5−2μm) and uniformity. After spray deposition, the substrates were left to cool down naturally in ambient conditions. Spray deposited film was dry at 400 ℃. Selenization of the spray deposited wz-CIS films were carried out in a tube furnace in Ar atmosphere at 550℃. The samples were allowed to cool naturally in the tube furnace after the selenization process. On the top of the absorber layer, CdS film was deposited by chemical bath deposition (CBD) of thickness ~100 nm at the bath pH varying between 7-10, while window layers (i-ZnO (about 60nm) and Al-ZnO (around 250nm)) were deposited by the RF magnetron sputtering. Finally, gold electrode was deposited by thermal evaporation to complete the cell structure.

VII.5 Results and Discussion

VII.5.1 Absorber Layer wz-CIS and ch-CISSe

Initially, wz-CIS ink was spray coated on SLG substrates using nitrogen as carrier gas to optimize the film quality and uniformity. 260 mg of wz-CIS NPs were dispersed in mixture of 20 ml toluene and varying quantity (2, 4, 6 and 8 ml) of 1-

DDT solvent. Hereafter, the ink prepared with 2, 4, 6 and 8 ml 1-DDT will be referred to as A, B, C and D ink, respectively. **Figure VII.1** shows the morphology of the spray deposited wz-CIS and selenized ch-CISSe films. To produce a homogeneous layer of wz-CIS, substrate temperature should be high enough to ensure the removal of solvent (toluene and 1-DDT) upon interaction with the substrate surface. Typically, the formation of a nonhomogeneous layer is due to very low substrate temperature,not enough to evaporate the solvent resulting in the formation of ink droplets on the substrate. On another hand, if substrate temperature is too high the solvent evaporates before reaching the substrate resulting in the formation of particle aggregates [252, 292]. Therefore, during spray coating, the substrate temperature was carefully adjusted. When ink A was deposited at 250 ^{o}C, a uniform coating with a large number of cracks formed as shown in **Figure VII.1(a) and (b)**. During drying step, the excess solvent (toluene and 1-DDT) evaporated and film shrunk, this shrinkage was the primary reason for the crack formation. Although, grain size increased on selenization, the cracks remained and became wider as shown in **Figure VII.1(b) and (c)**. Some minor cracks could close due to expansion during selenization (marked with a rectangle box in **Figure VII.1(c)**). When 1-DDT solvent amount was increased to 4, 6 and 8 ml in the ink, cracks increased while the coverage of the films became poorer in as deposited condition as shown in **Figure VII.1(d)**, **(g)** and **(j)** (sample B, C and D). The addition of 1-DDT increased the ink viscosity resulting in nonuniform coverage, while the slower evaporation rates restricted the solvent removal during deposition, thereby, promoting the crack formation during drying. Selenization results in partial substitution of Se for S in CIS structure, as discussed in chapter VI. Selenium being larger than S, when substituted results in lattice expansion thereby closing some of

the minor cracks. The presence of larger cracks could not be closed during selenization. It was interesting to observe that the presence of greater amounts of sulfur source, 1-DDT, promoted the grain growth during selenization. The higher grain growth was observed in the sample D where 8ml 1-DDT was added in the ink.

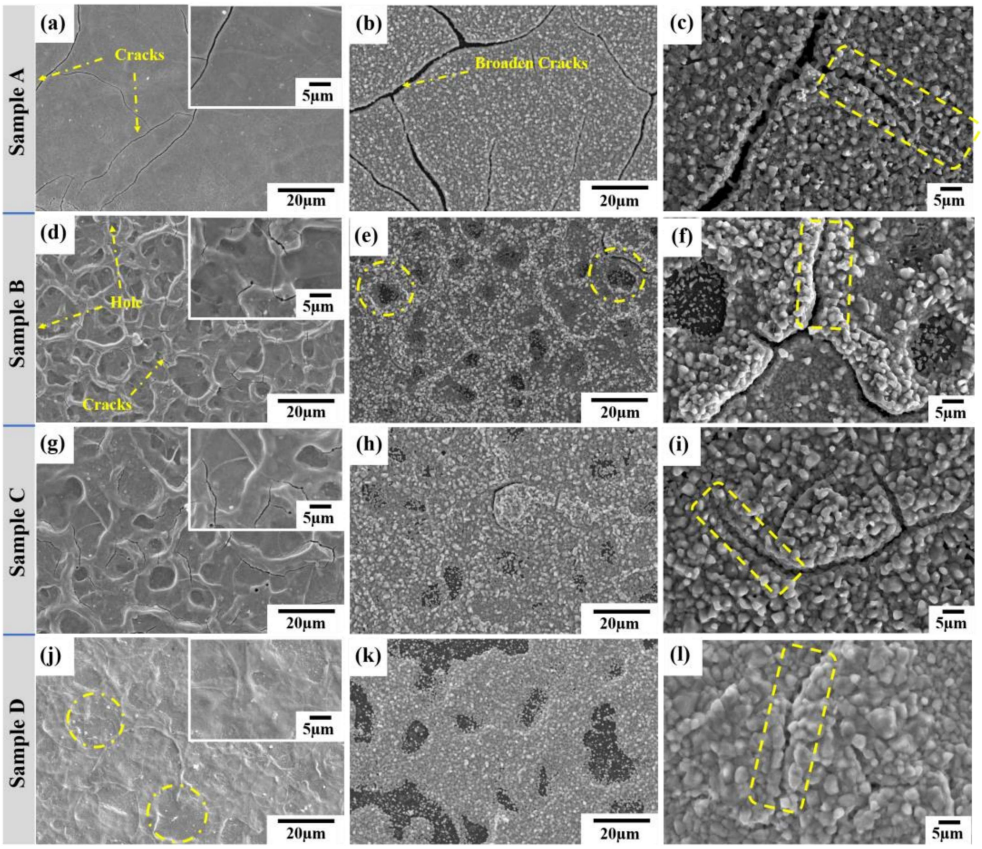

Figure VII.1 SEM images of as-deposited CIS thin films obtained using different spray conditions: variation of 1-DDT solvent (a) 2ml, (d) 4ml, (g) 6ml and (j) 8ml, substrate temperatures 250 ºC for (a) and 300 ºC for (d, g, and j), SEM image of selenized sample(A-D) at 550ºC for 15 minutes such as (sample A (b, c), sample B(e, f), sample C(h, i), sample D(k, l).

Generally, cracks forms due to shrinkage of film, agglomeration of particles and high concentration of ink. Diluting the ink would reduce the thickness per pass during deposition, which would allow evaporation of the dispersant solution during spray deposition, while any crack developed due to evaporation would be filled effectively during subsequent spray passes [295].

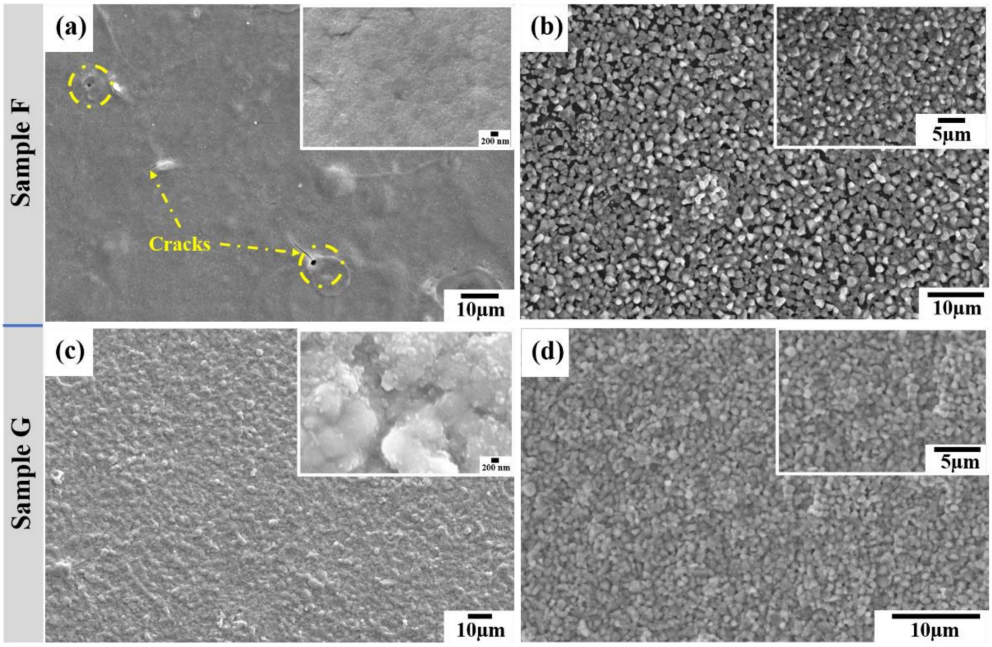

Figure VII.2 SEM images of (a, c) as-deposited wz-CIS and (b, d) selenized ch-CISSe thin films obtained using different spray ink concentrations: sample F and G that has set the inorganic load of inks prepared from wz-CIS NPs to 3.4 mg/ml and 2.8 mg/ml respectively.

For improving the surface and getting rid of crack formation, the ink was diluted. Samples F and G were prepared using wz-CIS NP ink having 3.4 mg/ml and 2.8 mg/ml loading, respectively. Further, agglomeration of particles was avoided by increasing probe sonication time to 300 seconds and power of sonication to 250W.

The films deposited using diluted ink F and G are shown in **Figure VII.2(a) and (c)**, respectively. The as-deposited sample F had cracks and pinholes as shown in **Figure VII.2(a)**, while the high- resolution image (inset **Figure VII.2(a)**) show non-uniform deposition. The porosity can also be observed in the selenized sample, where the grain growth happened in a scattered manner **(Figure VII.2(b))**. In the case of Sample G, a dense and uniform morphology without any pin holes and cracks was obtained **(Figure VII.2(c))**. which after selenization resulted in compact ch-CISSe layer without any pin hole or porosity as shown in **Figure VII.2(d)**.

After achieving the dense ch-CISSe films on SLG substrate, the CIS ink was deposited on SLG/Mo substrate to fabricate the absorber layer for device fabrication. Presence of Mo over the SLG substrate raises two more important concerns; I) oxidation of Mo film during spray pyrolysis and II) delamination of Mo layer during selenization.

Oxidation of the bare Mo layer during absorber deposition is a phenomenon that is difficult to avoid [60, 296]. Reports have shown that surface oxidation of the Mo layer results in the loss of conductivity and reflectivity [297]. It can also prevent the formation of a beneficial interfacial $MoSe_2$, which improve the adhesion of absorber layer with back contact [298]. In addition, MoO_x layer act as a barrier for sodium diffusion from the substrate to the CIS layer and thus the availability of Na during the CIGSe growth process is affected, hampering the overall device performance [299]. To obtain optimum deposition temperature, the stability of Mo layer over SLG was analysed in ambient atmosphere over a range of temperature. The X-ray diffraction recorded after annealing at different temperatures in an open atmosphere is shown in **Figure VII.3(a)**. When annealed at temperature 250 ^{o}C,

single phase crystalline Mo was intact , however, as temperature increased to 300 ^{o}C and 400^{o}C, extra peaks corresponding to MoO_x (ICSD: 99714, 86426) was observed indicating to the oxidation of Mo layer. Therefore, in order to avoid any oxidation of Mo film during spray deposition the temperature was kept below 250 ^{o}C.

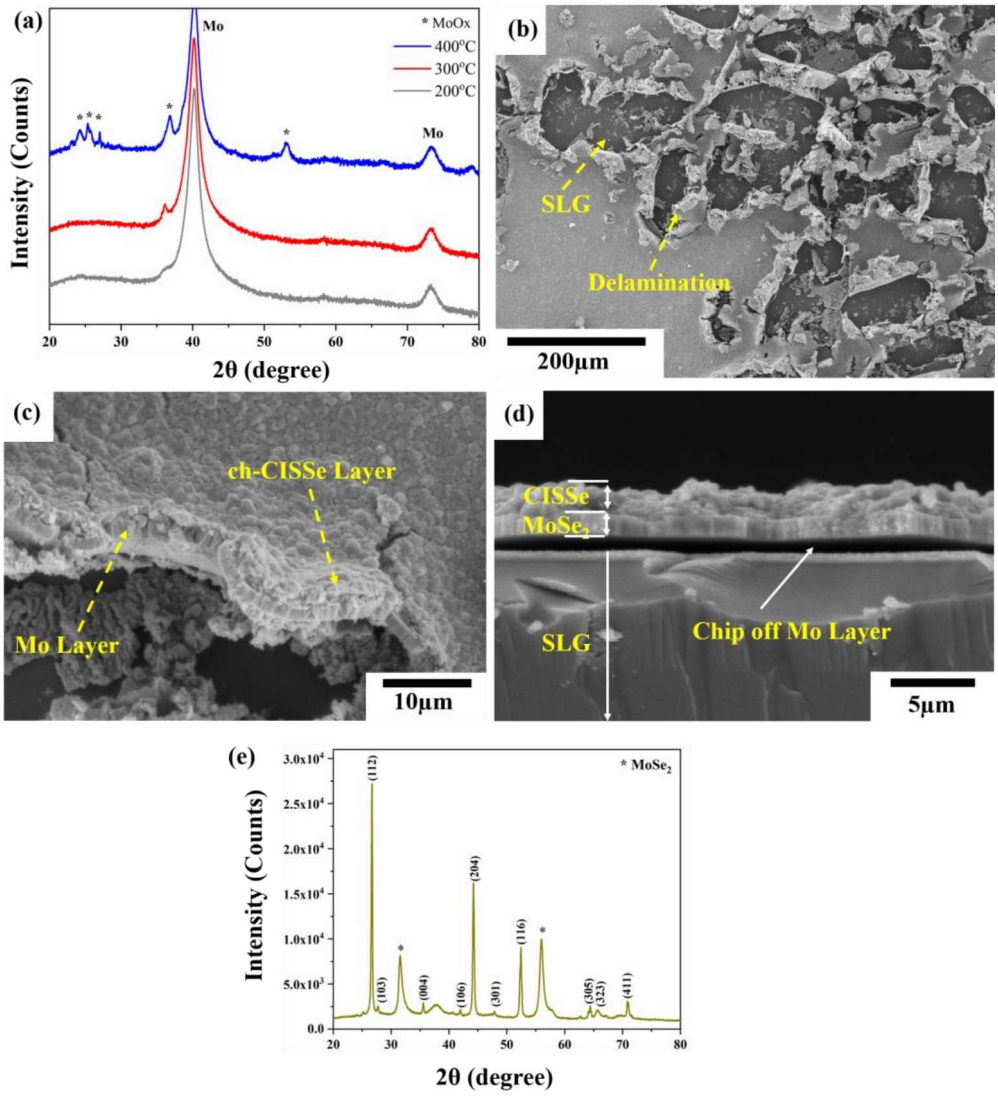

Figure VII.3 (a) X-ray pattern of molybdenum coated soda-lime glass at different annealing temperature, (b-c) Top view, (d) Cross-section of delamination of the

Mo/CISSe from the glass substrate after selenization, (e) XRD pattern of thick layer of $MoSe_2$ layer.

Another issue is delamination of Mo layer that was observed during selenization. This could be due to the thermal expansion mismatch between SLG and Mo on heating during selenization or oxidation of Mo layer due to trapped moisture/oxygen during deposition [300] and Na diffusion from the glass [301]. In this case, the delamination of Mo layer was found to be due to the presence of oxygen molecules, which oxidized the film or most likely excessive formation of $MoSe_2$ layer, which has been also discussed in literature [300, 302, 303]. $MoSe_2$ forms at Mo/CIGS interface during selenization. Delamination and high series resistance due to excessively thick $MoSe_2$ is a widely reported issue in solution-processed CIGS solar cell [301, 304, 305]. The existence of an interfacial $MoSe_2$ layer has been frequently reported; however, its role in terms of structure, thickness, and electrical behaviour is still a topic of debate [77, 78, 306, 307]. **Figure VII.3(b) and (c)** shows an image of Mo/CIS film delamination from the glass substrate observed in the present work. The cross-section of the SEM image clearly shows the chip-off of Mo/CIS layer from SLG **(Figure VII.3(d))**. It was supported by the XRD pattern that shows the presence of $MoSe_2$ phase **(Figure VII.3(e))**. In this case, three shots of selenium (each shot weight ≈ 48 mg) as selenium source, while the argon flow of 2-5 sccm was maintained during selenization at 550°C for 15 min. Changes in the selenization protocols were made to avoid the delamination during selenization which included: (I) carefully adjusting the amount of selenium (Se), to achieve optimum Se weight to film size ratio i.e. two shots of Se for 2 cm x 2 cm Mo/wz-CIS size, (II) preheating the substrates to 120 °C in the tube furnace

under vacuum for 10 minutes to remove any adsorbed moisture or oxygen , and III) increasing the flow rate of argon to 20 sccm. These measures significantly improved the adhesion of Mo/CIS to SLG as shown in **Figure VII.4**.

Finally, we made the spray coating of wz-CIS on Mo coated SLG substrates at 250 ^{o}C with nitrogen as a carrier gas using 2.8 mg/ml w-CIS nanoparticle. The cross-section SEM image of spray deposited wz-CIS film is shown in **Figure VII.4(a)**. The deposited wz-CIS film was nearly uniform, having a dense structure without cracks or pinholes. The film thickness deposited by spray coating was 1.8±0.2 μm while the elemental Cu:In:S ratio estimated using EDS was 1.0:0.80:2.60. The cross-sectional view of the selenized ch-CISSe layer showed large-grained (grain size=558±86 nm) and compact microstructure having a thickness of around 2.0±0.2 μm as shown in **Figure VII.4(b)**. The elemental Cu:In:S:Se of the ch-CISSe estimated to be 1:0.87:0.06:2.11.

XRD pattern of the spray-deposited wz-CIS film and selenized ch-CISSe films **(Figure VII.4(c))** showed phase pure crystalline wz-CIS and ch-CISSe, respectively. The XRD pattern of chalcopyrite did not show any peak related to $MoSe_2$ or it may be below the detection limit of XRD. To check the presence of any binary phase (such as Cu-S or In-S) in the sprayed wz-CIS and selenized ch-CISSe films, Raman spectroscopy was carried out in the wavenumber range 100-500 cm^{-1}. Raman peak position and vibrational mode are shown in **Table VII**.1. Generally, the most intense vibration bands of the wz-CIS compound are detected in the range of 255–360 cm^{-1} [230, 308]. In wz-CIS film dominant Raman peak at 296 cm^{-1} can be attributed to the signature A_1 mode of wz-CIS with the one additional shoulder peak at 331 cm^{-1} attributed to the E(T) transverse mode **(Figure VII.4)** [309]. The

typical Raman vibration peaks of Cu_2S (472 cm^{-1}) and CuS (474 cm^{-1}) and other known binary phases were absent [310]. On selenization, ch-CISSe film showed the main peak at 173 cm^{-1} attributed to the A_1 mode. It confirms the formation of the phase pure chalcopyrite CISSe. It was observed that the peak at 173 cm^{-1} was offset from the peak reported at 175−176 cm^{-1} on CISSe film formed through another approach, possibly because of the different S/Se ratios [311, 312]. In addition to the A_1 mode, the broad hump centered at 237 cm^{-1} was related to B_2/E mode that corresponds to the ch-CISSe [313]. Generally, Raman peak of the binary CuSe phase was reported at 260 cm^{-1} which was not detected in this case.

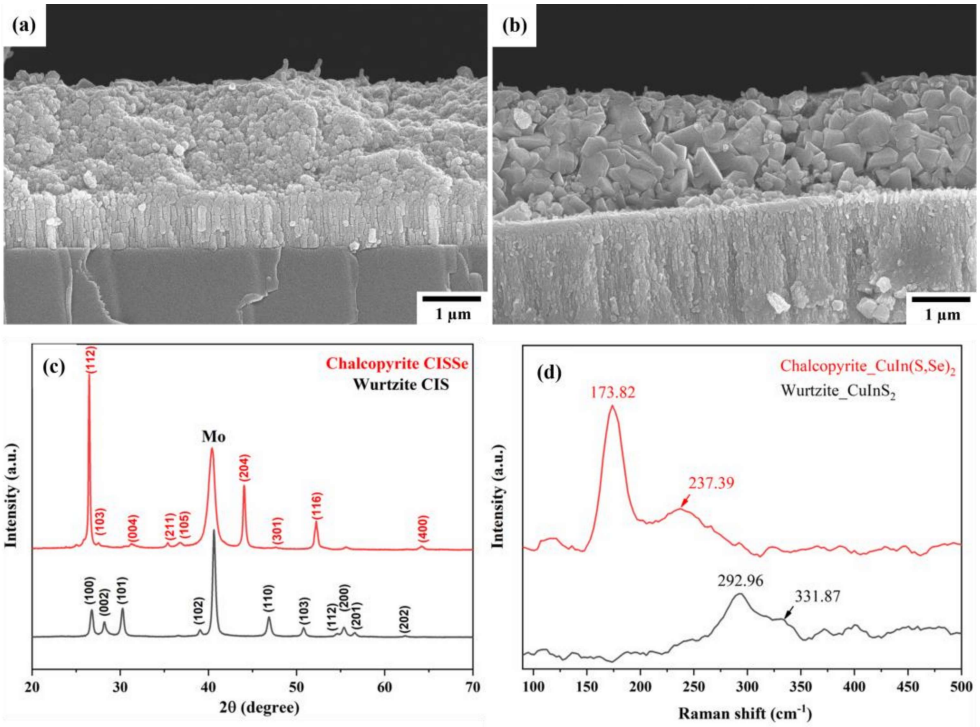

Figure VII.4 FE-SEM image of a cross-section view of (a) wz-CIS and (b) ch-CISSe, respectively, (c) X-ray diffraction pattern, (d) Raman spectra of the sprayed wz-CIS and selenized ch-CISSe thin film on soda-lime glass.

Table VII.1 List of Raman peak position and vibrational mode for chalcopyrite-CISSe and wurtzite-CIS.

Structure	Peak Position (cm^{-1})	Mode
Chalcopyrite ($CuIn(S,Se)_2$)	173.82	A_1 mode
	237.39	B_2/E mode
Wurtzite ($CuInS_2$)	292.96	A_1 mode
	331.87	E(T) transverse mode

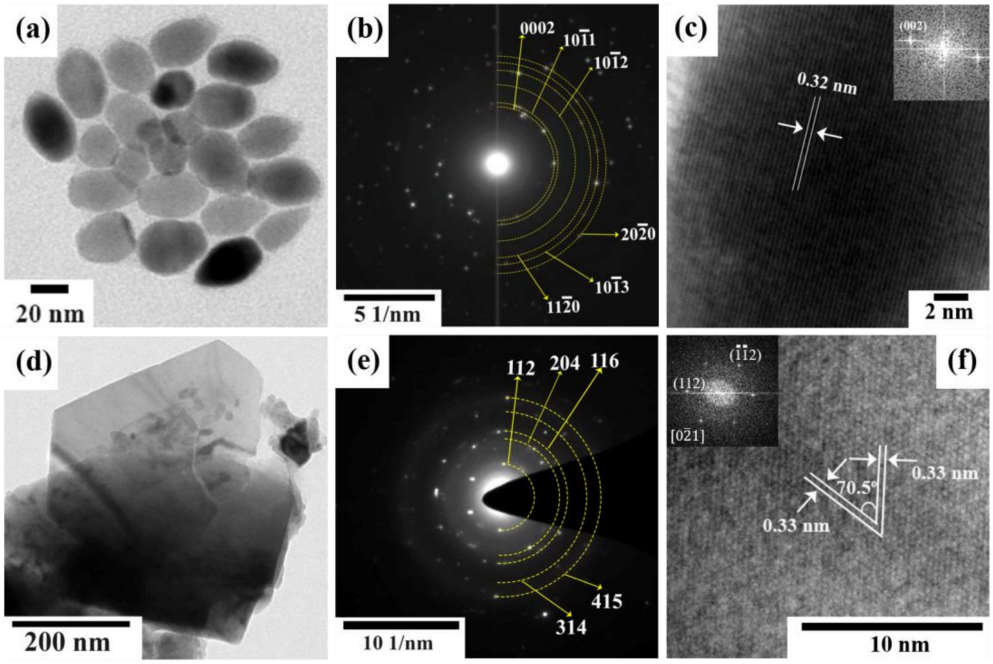

Figure VII.5 (a) Bright field TEM image (b) SAED pattern and (c) HRTEM image of sprayed CIS, (d) Bright field TEM image (e) SAED pattern and (f) HRTEM image of selenized ch-CISSe.

In order to further clarify crystal structure of the produced wz-CIS and selenized ch-CISSe, TEM was used. The bright-field image of wz-CIS had a uniform particulate shape with an oval morphology having a mean diameter and length of 20.69 ± 0.58 and 25.15 ± 1.23 nm, respectively **(Figure VII.5(a))**. The diffraction

rings consist of many discrete spots corresponding to crystallographic planes (0002), (10$\bar{1}$1), (10$\bar{1}$2), (11$\bar{2}$0), (10$\bar{1}$3) and (20$\bar{2}$0) of wz-CIS **(Figure VII.5(b))**. The observed d-spacing of the dark-contrast domains was 0.32 nm by high-resolution TEM (HRTEM), which was close to the spacing of (0002) plane of the wz-CIS **(Figure VII.4(c))**. In contrast to wz-CIS, the TEM images obtained for the ch-CISSe had an irregular shape as shown in the **Figure VII.5(d)**. The diffraction rings were indexed to (112), (204), (116), (314) and (415) planes of tetragonal (space group $I\bar{4}2d$) ch-CISSe phase **(Figure VII.5(e))**. The d-spacing of 0.33 nm between the lattice fringes observed in HRTEM image **(Figure VII.5 (f))** were close to the d-spacing of (112) and ($\bar{1}$12) planes of Ch-CISSe. The angle between the (112) and ($\bar{1}$12) planes was measured to be 70.5° **(Figure VII.5(c))**. These results are in agreement with the reported literature[172, 293, 314].

To elucidate the elemental oxidation states of the incorporated selenium atom during selenization, XPS spectra of the CIS films before and after selenization were carried out (**Figure VII.6)**. The survey spectrum of wz-CIS indicated the presence of Cu, In, and S elements as along with C and O as shown in **Figure VII.6(a)**. In ch-CISSe, an additional peak of Se was observed after the selenization. The binding energies (BE) were calibrated using the C 1s (284.80 eV) as reference [315]. High-resolution XPS spectra of Cu 2p, In 3d, and S 2p for wz-CIS and ch-CISSe films are shown in **Figure VII.6(c)**, **(d)** and **(e)**, respectively. The presence of two intense peaks centered at the BE of 932.70 eV and 952.50 eV with a peak splitting of 19.80 eV [176] correspond to the Cu $2p_{3/2}$ and the Cu $2p_{1/2}$, respectively of Cu^{1+} state **(Figure VII.6(c))** [94, 308]. The two peaks centred at 444.90 and 452.50 eV, with a spin orbital peak splitting of 7.60 eV [176], were attributed to trivalent indium. It

is observed that FWHM of In $3d_{5/2}$ peak increased after selenization, which needs further investigation. The broad peak at around 162 eV obtained from wz-CIS films, corresponding to the S 2p could be deconvoluted **(Figure VII.6(e))** into two components centred around 161.80 eV and 162.95 eV belonging to the S $2p_{3/2}$ and S $2p_{1/2}$ with the spin orbital splitting of 1.1 eV and was attributed to the S^{2-}.

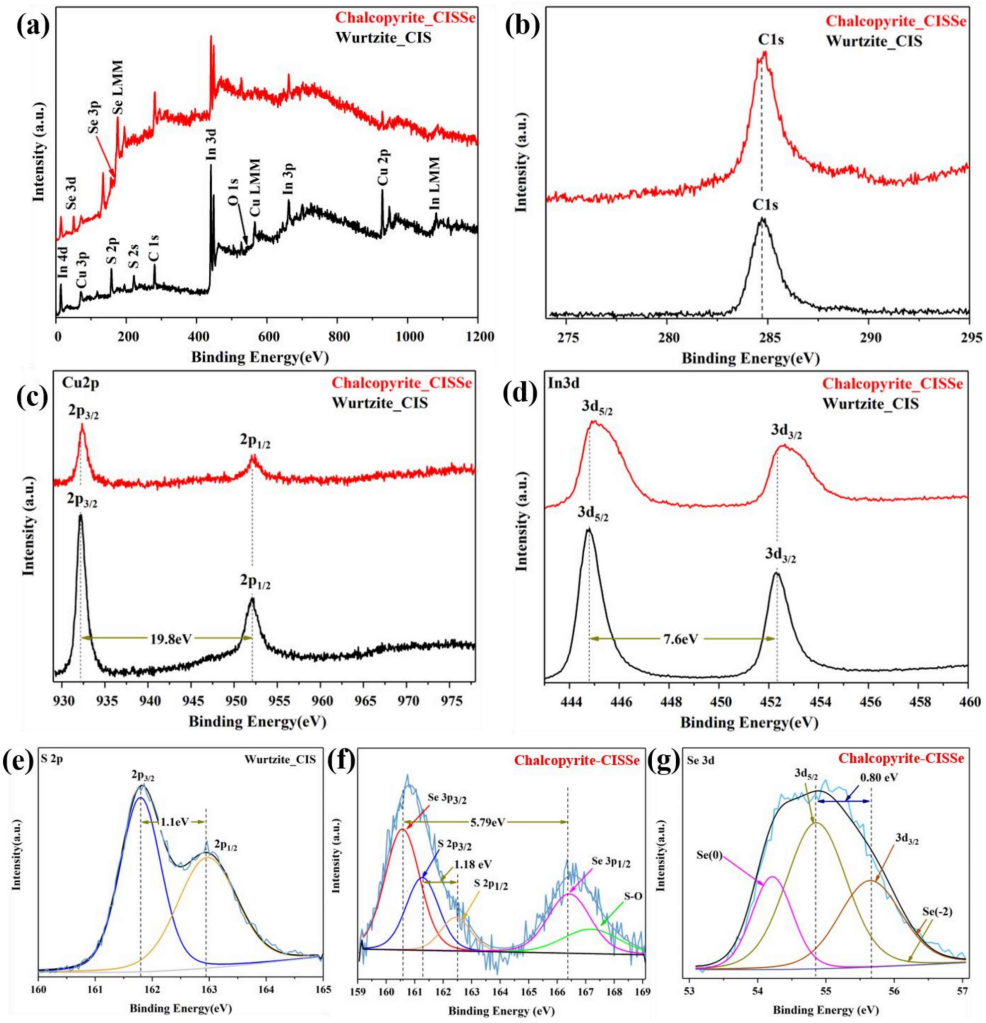

Figure VII.6 XPS spectra of (a) survey spectrum (b) C 1s (c) Cu 2p (d) In 3d of CIS films before(wz-CIS) and after selenization(ch-CISSe), (e) XPS spectra of S 2p of wz-CIS, (f) XPS spectra of Se 3p and 3d of ch-CISSe film.

After selenization additional peak at BE of 166.5 eV appeared along with a broad peak centered at 160.75 eV. The peak 166.39 eV was attributed to the Se $3p_{1/2}$ while the broad peak at 160.75 eV encompassed Se $3p_{3/2}$ and S 2p peaks. Therefore, the peaks were deconvoluted into several components as shown in **Figure VII.6(f)**. This confirmed that a fraction of sulphur remains after selenization. The deconvoluted component peaks at BE 161.27 eV and 162.45 eV ($\Delta E \approx 1.18$ eV) was attributed to S $2p_{3/2}$ and S $2p_{1/2}$, while peaks at 160.60 eV and 166.39 eV with an spin orbital splitting $\Delta E=5.79$ were from Se $3p_{3/2}$ and Se $3p_{1/2}$ [316]. A slight shift (of about 0.03 eV) in S $2p_{3/2}$ peak positions towards higher BE was observed on selenization. This could be attributed to the fact that selenium binds more strongly with Cu and In. The Se 3d orbital can be deconvoluted into three distinct peaks representing two different states **(Figure VII.6(g))**. The two different states, noting Se^{-2} split energy peaks at 54.84 eV and 55.64 eV with Se 3d spin-orbit splitting of 0.80 eV [317], and the broad component peak centered at 54.19 eV was attributed to the metallic Se(0). Se^{-2} originated from CISSe phases while Se (0) was due to condensation of Se vapour over the film or grain boundaries. For CZTS, excess selenium was reported to increase the bandgap of kesterite CZTS and widen the space-charge width, which improves the charge carrier density [318]. However, in this case, the effect of the presence of excess Se needs to be investigated.

The optical absorption of the as-deposited wz-CIS and selenized ch-CISSe film were investigated by UV-Vis diffuse reflectance spectroscopy. The wz-CIS film begins to weakly absorb at wavelength 1400 nm. The absorption increases slowly as wavelength is reduced. This could be due to the Urbach tail. A strong absorption is observed in the wavelength range 750-400 nm. The absorption begin as the

energy of photon approaches the bandgap energy of the wz-CIS. Any energy greater than that of bandgap was absorbed. However, as the photon energy approaches 400 nm (~3.1 eV) absorption decreased due to the presence of a relatively lower number of states for absorption to occur **(Figure VII.7(a))**, whereas the ch-CISSe film interestingly shows broad absorption ranges from 1300 to 450nm, with highest absorption at around 1100 nm **(Figure VII.7(b))**. The bandgap was estimated using the Kubelka-Munk function plot. Kubelka-Munk function: $\alpha/S = (1-R)^2/2R$, where α, S and R are absorption coefficient, scattering coefficient reflectance respectively. The band edge of wz-CIS and ch-CISSe films were around 1.54 eV ($\lambda \approx 806$ nm), inset image **Figure VII.7(a)** and 0.97 eV ($\lambda \approx 1278$ nm) insert image **Figure VII.7(b)** respectively, which was in agreement with the earlier reports [172, 319]. The E_g values, obtained in this case, slightly deviated from reported literature [172, 319] which might be due to the defect concentration or crystalline sizes or the presence of trace impurities.

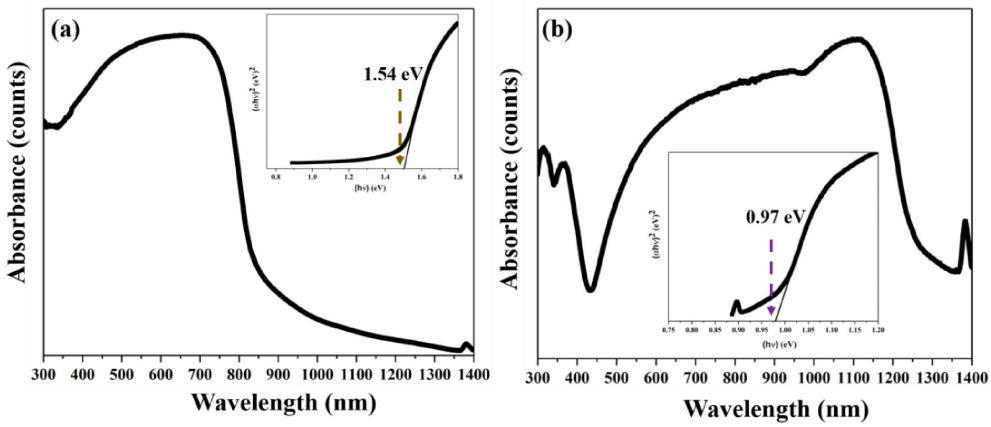

Figure VII.7 Absorption spectra and Tauc plots (in the insert) of (a) wz-CIS (b) ch-CISSe film.

As we discussed in chapter II, the typical wz-CIS can be made either p-type or n-type semiconductor material depending on the variation of copper and sulfur introduced during the preparation of nanoparticles. The Hall effect measurements at room temperature of the as-deposited wz-CIS and selenized ch-CISSe was carried out to measure the resistivity and carrier concentration, which is listed in **Table VII.2** A positive Hall coefficient (R_H) indicated to the p-type character of both wz-CIS and ch-CISSe layers. The sheet resistivity, mobility and carrier concentration were $1.76x10^4$ Ω/ cm^2, 1.27 cm^2/V-s and $2.79x10^{14}$ /cm^3 respectively for as-deposited wz-CIS, which was comparable to the reported values [225]. The sheet resistivity, mobility and carrier concentration of the ch-CISSe were $1.64x10^2$ Ω/cm^2, 1.53 cm^2/V-s and $2.49x10^{16}$ /cm^3 respectively, which was superior than the wz-CIS and comparable to the reported values [320–322]. Enhancement in the electrical properties after selenization could be attributed to the phase transformation, improved crystallinity and grain growth resulting in decrease in the defect concentration and pores.

Table VII.2 Electrical parameters of wz-CIS and ch-CISSe were calculated from Hall effect measurement.

Structure	**Conduction type**	**Hall Coefficient (cm^3/C)**	**Sheet resistivity (Ω/cm^2)**	**Mobility (cm^2/V-s)**	**carrier conc. (1/cm^3)**
WZ-CIS	p-type	2.23E+04	1.76E+04	1.27	2.79E+14
CH-CISSe	p-type	2.50E+02	1.64E+02	1.53	2.49E+16

VII.5.2 Buffer Layer Deposition by CBD

Cadmium Sulfide (CdS) was used as buffer layers for wz-CIS and ch-CISSe absorber layers in the heterojunction solar cell. Optimization of deposition parameter of CdS layers was carried out on SLG substrate, which was later deposited on the absorber layer. CdS thin films were deposited on SLG substrates by chemical bath deposition (CBD) technique at bath pH varying from 8 to 11. Scanning electron microscopy revealed that the morphology, grain sizes and the yield of the CdS thin films were strongly dependent on the bath pH. At bath pH8 **(Figure VII.8(a))**, the thin film was porous, and the coverage was not uniform **(Figure VII.8(b))** with clusters of average size 47 ± 18 nm. The primary gains in the cluster were in the range of 21 ± 3.3 nm. The average (of more than five different points) Cd:S atomic ratio obtained from EDS was ~ 5:1. On increasing the bath pH to 9, the grain size of CdS thin films decreased slightly to 16 ± 3 nm, while the average size of clusters was 48±9 nm **(Figure VII.8(c))**. With increasing pH, the Cd/S ratio improved to ~ 1.7; however, the deposited films were still non-uniform and had a poor coverage **(Figure VII.8(d))**. On increasing the pH to 10, nearly stoichiometric CdS (Cd/S ratio close to 0.95) thin film formed with much-improved surface morphology coverage with fewer cracks and pinholes **(Figure VII.8(e), (f))**. The homogeneous and dense films were composed of clusters (51 ± 6 nm) having grains sizes 14 ± 3 nm. On increasing the bath pH to 11, the yield of CdS reduced while the grain and cluster sizes were about 12 and 53 nm, respectively (**Figure VII.8(g)**). The lower yield was due to the strong alkaline solution, which resulted in the formation of greater amounts of $Cd(OH)_2$ when compared to Cd^{2+} ion concentration. As a result, the coverage of the films was again hampered **(Figure**

VII.8(h)) while a non-stoichiometric film with Cd/S ratio close to 0.80 was obtained. Therefore, based on the observations, the bath pH of 10 yielded the best results.

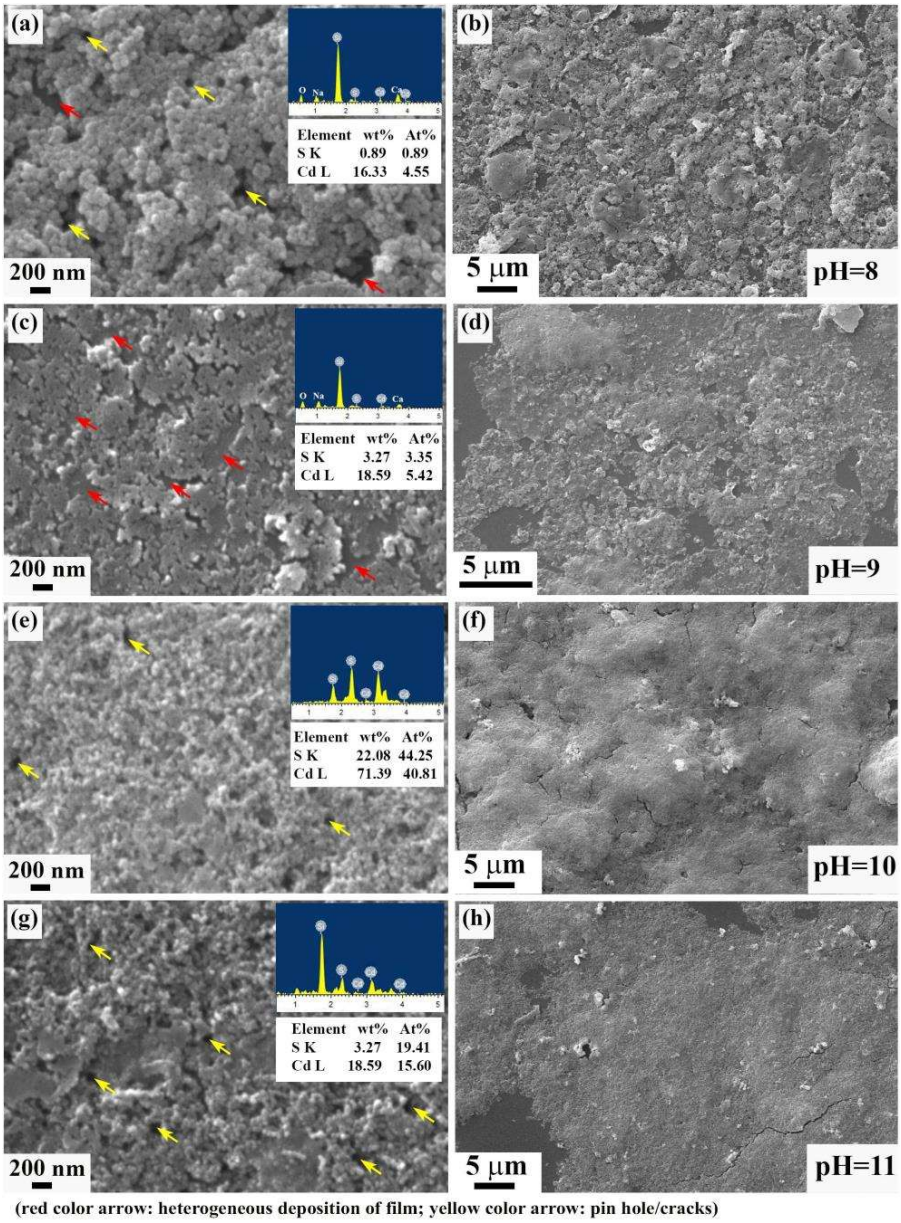

Figure VII.8 SEM micrograph of the CdS thin films deposited on the glass substrate at (a-b) pH 8, (c-d) pH 9, (e-f) pH 10 and (g-h) pH 11 and corresponding EDS spectra.

During CBD, CdS film can grow by two different mechanisms: i) ion by ion condensation of Cd^{2+} and S^{2-} on the substrate when ionic product of $[Cd^{+2}][OH^{-}] < K_{SP}$ of $Cd(OH)_2$ (K_{sp} = solubility product) that leads to the formation of $[Cd(NH^3)^4]^{2+}$ complex [323], forming a transparent, uniform and adherent film, ii) cluster by cluster deposition of particles which precipitate (due to formation of $Cd(OH)_2$ at higher pH) homogeneously in the bulk solution and are attached arbitrarily on growing film resulting in an opaque, non-uniform and poorly adherent film [323]. A schematic of the film formation mechanism during the CBD is depicted in **Figure VII.9(a)**. At the same time, higher pH favours quicker release of S^{2-} ions by the hydrolysis of $[(NH_2)_2CS]$. For a uniform deposition, it is necessary for $[(NH_2)_2CS]$ to release enough S^{2-} and Cd^{2+} ion from enough tetra-amine-cadmium ($[Cd(NH_3)_4]^{2+}$) complex attached to the surface of the substrate, which by ion-exchange forms CdS [323]. At lower pH of 8, lesser amounts of sulphur ions were released resulting in higher Cd/S ratio of ~ 5, which moved closer to the stoichiometric CdS with increasing pH (as a greater number of S^{-2} were released), and at a bath pH of 10, a stoichiometric CdS was obtained. On the other hand, when the bath pH was raised to 11, much greater amount of $Cd(OH)_2$ precipitated in the solution which formed CdS clusters by capturing S^{-2} from solution and got deposited on the already deposited CdS formed through $[Cd\ (NH_3)_4]^{2+}$ formation (which formed in lesser amounts) at the surface, resulting in non-uniform coverage of the film [324]. The XRD pattern of the CdS thin film deposited at varying bath pH is shown in **Figure VII.9(b)**. A background hump at $2\theta \approx 25\text{-}30°$ in all the XRD patterns was due to the glass substrate, while the broad peaks were from the nanocrystalline thin films. XRD pattern of the film obtained at pH10 could be indexed to wz-CdS phase (lattice constants, a = 4.1 and c = 6.67Å). At a lower pH

of 8, the presence of $[Cd(NH_3)_4]^{2+}$ complex promoted the formation of $(NH_4)_2Cd_2(SO_4)_3$. As pH was raised to 9, a greater amount of S^{-2} was released resulting in an increase in the formation of $(NH_4)_2Cd_2(SO_4)_3$ along with CdS. On the other hand, at pH 11, the formation of amorphous $Cd(OH)_2$ was promoted.

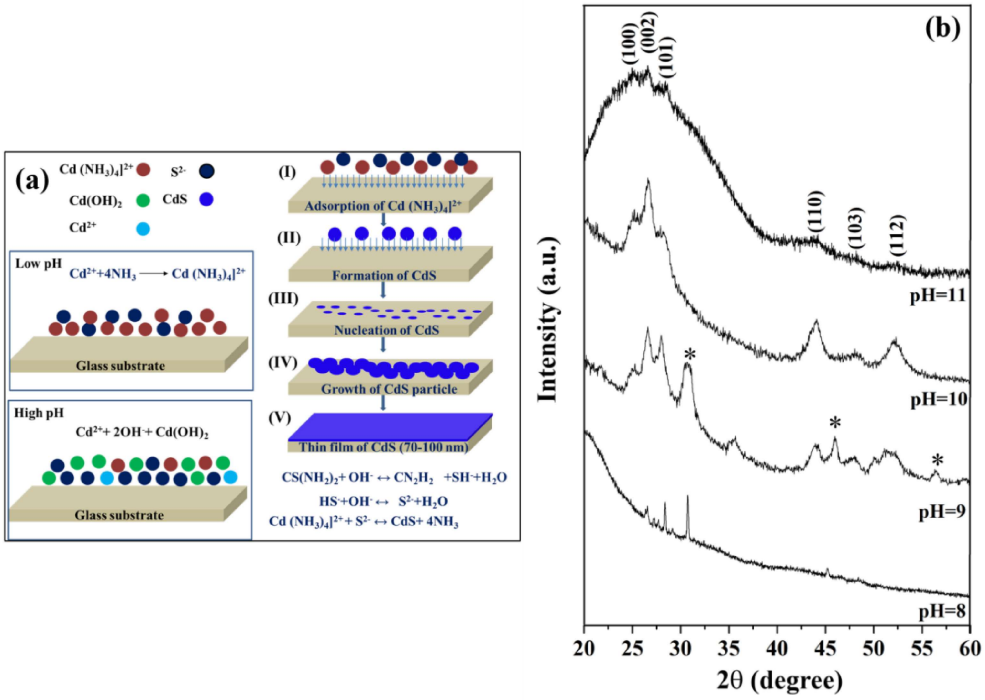

Figure VII.9 (a) Schematic of CdS film formation during CBD, (b) XRD pattern of the CdS thin films deposited at varying pH.

Absorption in the UV–visible region and bandgap is important for the applicability of the CdS thin films as buffer layer in solar cells. The absorption spectra **(Figure VII.10)** of the CdS thin films showed a blue shift with increasing bath pH. The optical bandgap (E_g) increased from 2.15 to 2.31 eV on increasing the bath pH from 8 to 11 **(Table VII.3)**. The thickness (t) of the films decreased from ~ 125 to ~ 83 nm, when the bath pH increased from 8 to 11 **(Table VII.3)**. This was probably due

to reduced concentration of the surface attached $[Cd(NH_3)_4]^{2+}$ with increasing pH (as explained earlier).

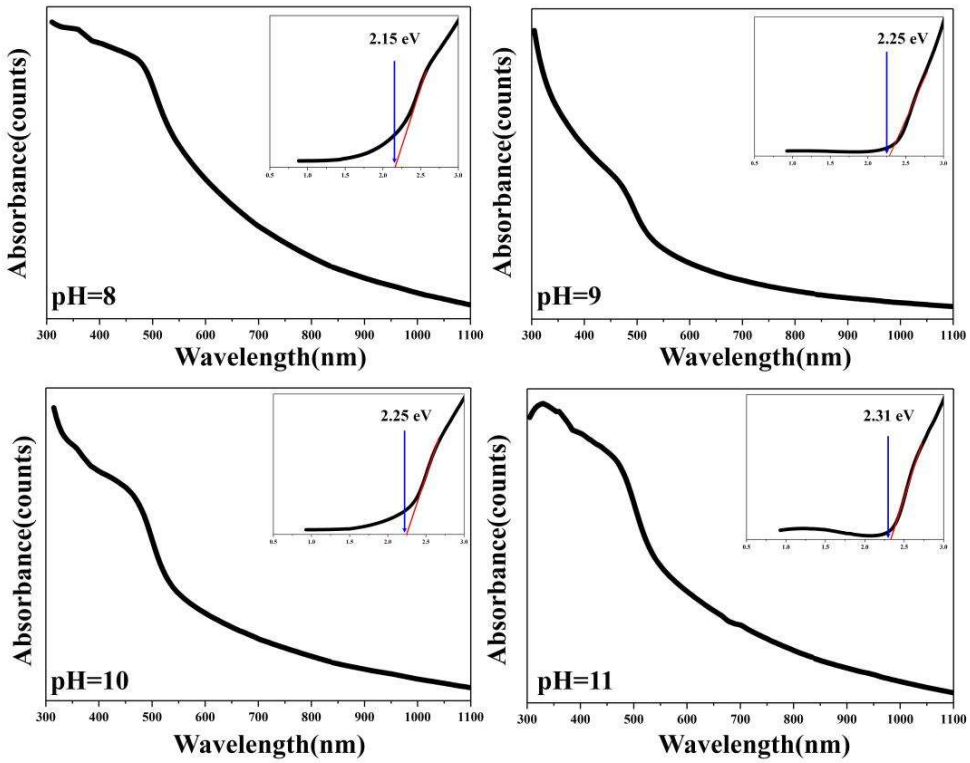

Figure VII.10 Absorption spectra of the CdS thin films deposited at varying pH.

The resistivity(q) of the CdS thin films decreased from 1.0 $x10^2$ to 3.0$x10^1$ Ωcm on increasing pH from 8 to 10 and again increased to 0.9$x10^2$ for pH11. The obtained bandgap and resistivity were comparable to the earlier obtained values using similar deposition techniques **(Table VII.3)**. Close to 100 nm thin CdS film with optical bandgap 2.25 eV, and resistivity 3.01$x10^1$ Ωcm, suitable for a buffer layer, was obtained in case of the bath pH 10.

Table VII.3 Thickness, bandgap and resistivity of the CdS films obtained in present and earlier studies using similar deposition technique.

Cadmium source	Other reagents used in solution	pH	Annealing				t (nm)	BG (eV)	ρ (Ω-cm)	Ref.
			Temp. (°C)	Time (min)	Atm.	method				
$CdAc_2$	NH_4Ac_2, $NH_4(OH)$, DI water	---	400	~8	vacuum	Convectional and RTA	~225-370	2.27	4	[325]
$CdCl_2$,	NH_4CI, TU	---	500	30	air	Convectional	250	---	$3x10^5$	[326]
			600	---	vacuum	RTA	250	---	0.16	
$CdSO_4$	N_2H_4, NH_3(25%), TU	9.4	150-550	60	nitrogen	horizontal tube furnace	2800	2.42 -2.28	$0.5x10^5$ - $0.1x10^1$	[327]
$CdCl_2$	$(NH_2)_2CS$, NH_3	10	450	5	vacuum	tubular furnace	400	2.46	0.1	[328]
							100	2.42	$4.4x10^5$	
$CdCl_2$	NH_4CI, TU, NH_3	---	200	60	vacuum	Convectional	>500	2.48	10	[329]
$CdCl_2$	$C_6H_5O_7Na_3$, KOH, TU, DI water	10	300	120	air	Convectional	85-220	2.33-2.39	$6.29x10^5$ -$4.05x10^6$	[330]
$CdSO_4$	N_2H_4, TU, NH_3(25%)	---	300	60	nitrogen	Convectional	700	2.33	$<6.0x10^{10}$	[331]
Properties achieved Present Study										
$CdAc_2$	TU, NH_3(25%), DI water	8	120	5	air	RTA	125	2.15	$\sim10^2$	
		9					96	2.25	$8.12x10^1$	
		10					99	2.25	$3.01x10^1$	
		11					83	2.31	$0.9x10^2$	

VII.5.3 Window Layer Deposited by RF Sputtering

The window layer consisting a thin (~ 60 nm) high-resistivity intrinsic zinc oxide (i-ZnO) layer followed by a thick (~ 300 nm), conductive Al-doped ZnO (AZO) layer. A large bandgap of the window layer i.e., i-ZnO was used to protect the underlying CdS from sputter damage from highly energetic particles during Al-ZnO deposition, and to avoid front surface recombination. Both the layers were deposited over the CdS layer by RF magnetron sputtering. Deposition parameters are mentioned in chapter III.

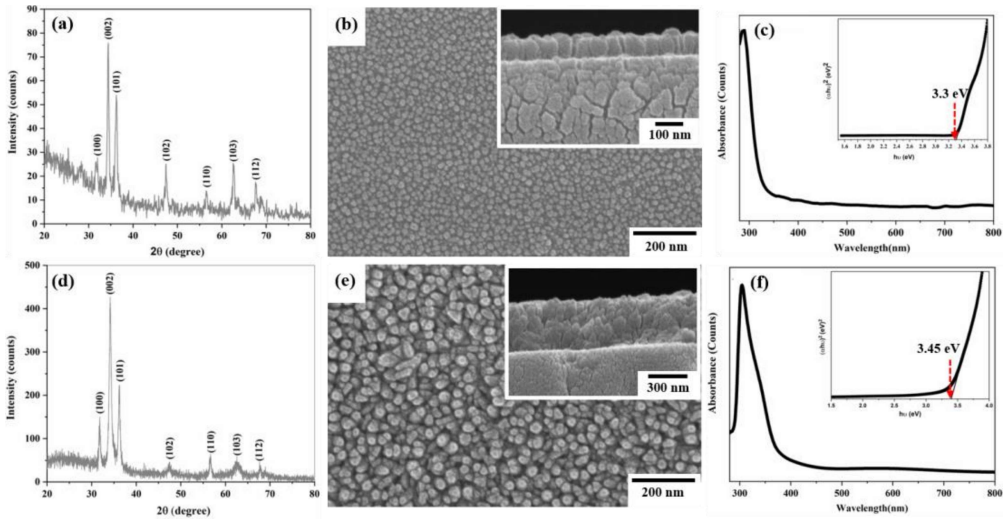

Figure VII.11 Grazing incident-XRD (a and d), SEM image (inset cross-section image) (b and e) and absorption band (inset bandgap diagram) (c and f) of sputtered ZnO and Al-ZnO layer.

Figure VII.11(**a** and **c**) shows the GIXRD patterns of the as-deposited ZnO and Al-ZnO films on SLG. Both the GIXRD patterns were indexed to the wurtzite structure which was matched with the reported literature [332–334]. A uniform morphology and grain size was observed in both i-ZnO and Al-doped ZnO films as shown in **Figure VII.11(b)** and **(e)** respectively. Compact and grains elongated along the thickness was observed in the cross-section of i-ZnO and Al-ZnO films as shown in the inset of **Figure VII.11(b) and (e)** respectively. UV-Vis spectrophotometer was used to characterize the optical properties of ZnO and Al-ZnO thin films in a range of 280-800 nm. Both films showed strong absorption in UV range below 350 nm wavelength. The absorption edge of the Al-ZnO film was shifted to the lower wavelengths when compared to the i-ZnO film. The observed shift in the absorption edge indicated to the substitution of Al^{3+} ions at Zn^{2+} sites, which injects free electrons in the conduction band increasing optical bandgap. The bandgap (E_g) of

i-ZnO and Al-ZnO films were estimated using the Tauc plot shown in the inset of **Figure VII.11(c) and (f)** respectively. The bandgaps of i-ZnO and Al-ZnO was estimated to be ~3.30 and 3.45eV, respectively.

Gold lines were utilized as the current collector at the top of the window layer. The Au line were deposited by thermal evaporation while the line pattern was achieved using a mask.

VII.5.4 $CuIn(S,Se)_2$ Device Characterization

Solar cells were fabricated using both metastable wz-CIS and selenized ch-CISSe absorber films. The current density-voltage measured using a Keithley 2450 and solar simulator model #SS30AAA-EM. The current density-voltage (J−V) curve is shown in **Figure VII.12(a and b)**. The wz-CIS solar cell had J_{SC} and V_{OC} of 22.41 mA/cm^2 and 132 mV, respectively. The obtained value of short-circuit current (Jsc=17.80 mA/cm^2) was comparable to the highest reported value (J_{SC}=22.41 mA/cm^2) [294] for solution processed absorber films [233, 293, 294]. However, the wz-CIS device suffered from low open circuit voltage (V_{OC}=132mV), possibly due to poor junction between the wz-CIS film and CdS layer, which could be due to the lattice mismatch of 6.2%. The lower V_{OC} could also be due to high defect concentration in bandgap and recombination at the p-n junction interface. Also, the film surfaces are generally rough in spray deposition and CBD, which contributes to a further decrease of the Voc. The calculated value of fill factor (FF=70%) was superior in comparison to the reported data [187, 294]. A reduction in series resistance and increasing the shunt resistance also impact on the FF [20] that need to further study. The PCE (η) of the solar cells fabricated from the as-deposited wz-

CIS was 2.127%. The small size of wz-CIS NPs was another reason for the poor performance of solar cells because the presence of grain boundary density that affect the charge collection. The highest efficiency reported for the wurtzite CIS based solar cell is 6.72% by Golobostanfard *et al.* through electrophoretic deposition technique [294]. The average PCEs obtained for wz-CIS based solar cells by various research groups is 2.515% [293, 294] which is close to that obtained in this case. To the best of our knowledge, this is the first report of spray deposited wz-CIS based solar cell.

A much better performance was observed for ch-CISSe based solar cell when compared to device fabricated using wz-CIS as absorber layer. The J_{SC}, V_{OC}, FF and PCE obtained for both wz-CIS and ch-CISSe solar cells listed in **Table VII.3**. There was a significant increase of Voc that could be because of better matching of lattice constants with buffer layer CdS [79], reduced defect density and increased grain size which helps in reducing the recombination losses thereby, improving the Voc [35]. The lower band gap (close to 1 eV) of tetragonal CISSe tends the increase the absorption ranges from 1300 to 450 nm, enhancing the current density. As a result, a higher PCE of 7.35% was observed for ch-CISSe solar cell. However, device showed a low current-density (Jsc) that can be attributed to the presence of oxygen, carbon, selenium residues, as observed in XPS analysis **(Figure VII.6 (a and b))**. The presence of impurities can act as recombination centers, hampering the effective charge carrier collection. It should also be noted that the CdS layer deposited in this study was slightly thicker to ensure uniform coverage of CIS layer which probably added to the series resistance.

Table VII.4 Performance of PV devices fabricated using wz-CIS and selenized ch-CISSe absorber layers.

Deposition method	Area [cm^2]	Open circuit voltage, Voc (V)	Short-circuit current density, Jsc (mA/cm^2)	Fill factor, % (FF)	PCE (η)
Wurtzite CIS					
Spray coating	0.39	0.132	22.41	0.70	2.12
Chalcopyrite CISSe					
Spray coating	0.39	0.560	25.64	0.52	7.35

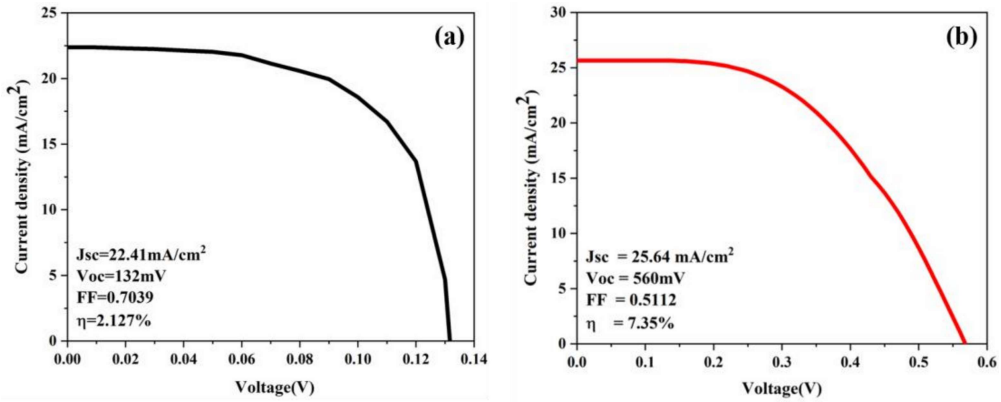

Figure VII.12 PV device response for a (a) wz-CIS and (b) selenized ch-CISSe with 2.12 and 7.35% power conversion efficiency respectively under AM1.5 illumination (100 mW/cm^2).

VII.6 Concluding Remarks

In this study, we have demonstrated wurtzite-CIS and chalcopyrite-CISSe based devices using the pre-synthesized wurtzite-CIS NPs ink. We showed that spray deposition at 250°C using a spray rate of 2ml/min, concentration of 2.8mg/ml (1-DDT: Toluene:: 1:10) produces a dense and uniform film. The delamination of molybdenum layer caused by formation of MoOx and excess formation of $MoSe_2$

were avoided on optimizing the selenization process. Selenization at 550 ^{o}C with 15 min hold produced micron size grains. XPS results showed the presence of elemental selenium which probably deteriorate the device's performance. Optical and electrical properties are superior in the case of ch-CISSe in comparison to wz-CIS. The wz-CIS solar cell fabricated from the spray-deposition CIS NPs layer on Mo substrate yield a PCE of 2.12%. For selenized ch-CIS based absorber layer, PCE improved significantly up to 7.35%.